

# Solute strengthening from first principles and application to aluminum alloys

G.P.M. Leyson<sup>a,\*</sup>, L.G. Hector Jr.<sup>b</sup>, W.A. Curtin<sup>c</sup>

<sup>a</sup> School of Engineering, Brown University, Providence, RI 02912, USA

<sup>b</sup> General Motors R & D Center, 30500 Mound Rd., Warren, MI 48090-9055, USA

<sup>c</sup> Institute of Mechanical Engineering, École Polytechnique Fédérale de Lausanne, Lausanne CH-1015, Switzerland

Received 13 February 2012; received in revised form 19 March 2012; accepted 19 March 2012

Available online 1 May 2012

## Abstract

Alloys containing substitutional solutes exhibit strengthening due to favorable solute fluctuations within the alloy that hinder dislocation motion. Here, a quantitative, parameter-free model to predict the flow stress as a function of temperature and strain rate of such alloys is presented. The model builds on analytic concepts developed by Labusch but introduces key innovations rectifying shortcomings of previous models. To accurately describe the solute/dislocation interaction energies in and around the dislocation core, density functional theory and a flexible-boundary-condition method are used. The model then predicts the zero temperature flow stress, the energy barrier for dislocation motion, and thus the finite temperature flow stresses. The model is used to predict the flow stresses of various Al alloys. Excellent results are obtained for Al–Mg and Al–Mn. Al–Fe with ppm levels of Fe is not predicted well but, using experimental results for Fe, results for the quasi-binary Al–Cr–(Fe) and Al–Cu–(Fe) alloys agree well with experiments. The model is also consistent with the “stress equivalency” postulate of Basinski. This parameter-free model using first-principles input thus provides a basis for achieving the long-sought goal of computational design of alloys, within the context of solute-strengthening mechanisms.

© 2012 Acta Materialia Inc. Published by Elsevier Ltd. All rights reserved.

**Keywords:** Ab initio calculations; Al alloys; Solute strengthening; Temperature dependence; Yield strength

## 1. Introduction

To facilitate the development of advanced materials, computational materials science can be used to create guidelines for design as well as give physical insight to experimentally derived trends. However, robust and predictive models are critical. Predictions of the macroscopic mechanical properties, such as flow stress, work hardening and fatigue behavior, in metals or other materials undergoing dislocation-mediated plastic flow hold particular challenges because the behavior is controlled by interacting phenomena

at multiple scales, from the atomic through the meso- and microstructural scales, and is associated with the collective interactions among defects (solutes, dislocations, grain boundaries, precipitates). In this paper, we consider the problem of solute strengthening, which combines the chemistry of solute interactions with dislocations in the host metal and the resulting configurations of the dislocation line. The fundamental interactions are on the Angstrom scale, but other characteristic scales, from 10 to 100 nm, control the overall material response. By capturing the phenomena at these scales, the model here provides a robust means for predicting the yield stress of solute-strengthened alloys, with application to Al alloys, as a function of composition, temperature and strain rate.

Solute-strengthened alloys, such as the 1xxx, 3xxx, 5xxx and solutionized 6xxx series aluminum alloys used in automotive applications, are some of the most

\* Corresponding author. Address: EPFL STI IGM-GE, ME B2 350 (Bâtiment ME), Station 9, Lausanne CH-1015, Switzerland. Tel.: +41 004 178 949 9726.

E-mail addresses: [gerard\\_paul\\_leyson@brown.edu](mailto:gerard_paul_leyson@brown.edu) (G.P.M. Leyson), [louis.hector@gm.com](mailto:louis.hector@gm.com) (L.G. Hector Jr.), [william.curtin@epfl.ch](mailto:william.curtin@epfl.ch) (W.A. Curtin).

technologically important materials in industry. The strengthening arises from the interaction of the eigenstrain created by the solutes with the stress field of the dislocation. If the solute is approximated as a point dilatational source at  $\vec{r}$  and the dislocation is at the origin, the interaction energy can be approximated by

$$U(\vec{r}) \approx -p(\vec{r})\Delta v_m \quad (1)$$

where  $\Delta v_m$  is the misfit volume of the solute and  $p$  is the dislocation pressure field exerted by the dislocation at the location of the solute [1]. Since  $p(\vec{r}) \sim 1/r$ , there is a gradient in the interaction energy that ultimately leads to dislocation pinning phenomena. Solute strengthening is typically divided into two classes: strong pinning and weak pinning. Regardless of the mechanism, the strengthening is a function of solute concentration  $c$ , the magnitude and gradient of the solute–dislocation interaction energies  $U(\vec{r})$ , the dislocation line tension  $\Gamma$ , the Burgers vector  $b$  and the shear modulus  $\mu$  of the matrix. These mechanisms have been characterized in classical studies [2–6], but, in spite of having a solid physical basis, quantitative parameter-free predictions remain elusive. The existing models also have features that are ill-defined, inhibiting predictability. For strong pinning, only the solutes along the glide plane are usually considered, even though the interaction energies of solutes off the glide plane can remain substantial in the vicinity of the dislocation. Applicability of the point pinning model at concentrations typical of engineering alloys (on the order of 1%) is questionable because (i) the distance between point pinning solutes, even just in the glide plane, is only a few Burgers vectors and (ii) for face-centered cubic (fcc) and some hexagonal close-packed (hcp) metals, wherein the dislocation core is split into partials that are separated by a nanometer or more, multiple solutes can be interacting with the dislocation in the same region. Furthermore, the total interaction energy  $U_{tot}$  of a dislocation line of length  $L$  lying along the  $z$ -direction is the sum of all individual solute/dislocation interactions. Since solutes with the same  $x$ - and  $y$ -coordinates have the same interaction energy,  $U_{tot}$  is given by

$$U_{tot} = \sum_{ij} n_{ij} U(x_i, y_j) \quad (2)$$

where  $n_{ij}$  is the number of solutes with position  $(x_i, y_j)$  perpendicular to the dislocation line. For random alloys, and for the  $1/r$  scaling of the energy with distance, the total energy can be divergent (although angular terms can lead to cancellation). The mean interaction energy of a dislocation in a random distribution of solutes is

$$\langle U_{tot} \rangle = \sum_{ij} \langle n_{ij} \rangle U(x_i, y_j) = cN \sum_{ij} U(x_i, y_j) \quad (3)$$

where  $c$  is the concentration of the solute and  $N$  is the number of atomic sites along the dislocation line. The mean energy  $\langle U_{tot} \rangle$  is thus independent of dislocation position as the dislocation moves from one atomic position to the next equivalent one, so that the configurational glide force  $f_c = -\partial \langle U_{tot} \rangle / \partial x$  due to the mean effect of the solutes is

then zero. Therefore, it is only the random fluctuations in solute concentration around the dislocation that can provide strengthening, and this is the genesis of the weak-pinning models. Segments along an initially straight dislocation can be attracted to energetically favorable fluctuations, and bow out towards them, at the cost of dislocation line energy, as discussed in the pioneering work of Labusch [5,7]. Difficulties arise, however, because the scaling of the energy fluctuations is proportional to  $(p\Delta v_m)^2$ , where  $p$  is the pressure field of the dislocation, thus depending on distance as  $r^{-2}$ , for which the summation over all solutes still diverges as  $\ln(R)$ , where  $R$  is the system size. To circumvent this problem, previous works have either arbitrarily set a finite interaction range or considered only solutes along the glide plane [5,7–14]. Predictions of such models depend on the ad hoc finite range of the interactions. Hence, no insight yet exists into selecting any “correct” range, or its possible dependence on alloy type or other material parameters. As noted above, ignoring solutes outside the glide plane is also not justified. Finally, none of the literature models account for solute interactions with the actual dislocation core structure.

Computer simulations based on continuum analysis [15–18] and molecular dynamics (MD) [12,19–23] have been developed to better understand the strengthening behavior of solute strengthened alloys. Continuum approaches have inherent limitations comparable to those associated with the corresponding analytic models. MD methods better describe the physics occurring in the core region, capture effects of solutes off the glide plane and permit the assessment of energy barriers to dislocation motion [12]. However, most studies do not capture the proper mesoscale dislocation configurations on the 10–100 nm scale (an exception being the numerical models of Provile and co-workers [19,22,23]) and all are limited to systems where the semi-empirical interatomic potentials for the alloy constituents are well established. First-principles calculations based upon density functional theory (DFT) capture both the mechanical and chemical processes occurring in the dislocation core [24–27], providing improvements over semi-empirical potentials and giving input for standard models. For instance, Yasi et al. [25] used a point-pinning model to predict basal-slip strengthening for various solutes in magnesium alloys, while Zander et al. [26,27] used first-principles calculations to determine the size and modulus misfit parameters of solutes in aluminum alloys and used this information in conjunction with the Labusch (weak-pinning) model [5,7] to develop a one-parameter strengthening model.

In this paper, we expand on a model first presented in Ref. [28] which addresses both the divergence of the fluctuations in the interaction energy and the interaction energy for solutes within the core of the dislocation for arbitrary solute additions to aluminum. The latter is addressed using DFT to compute the interaction energy of solutes in the immediate region of a core, the geometry of which is also computed fully within DFT using a flexible boundary

condition method. The former is addressed by following the general strategy of the Labusch model [5,7], but with a careful analysis of the concentration fluctuations that considers the spatial correlations in those fluctuations, which then leads to a parameter-free theory with no divergences and no ad hoc restriction on the range of solute/dislocation interactions. The resulting theory is applied to edge dislocations in Al–X alloys (X = Mg, Si, Cu, Cr, Mn and Fe) to predict the finite-temperature yield stress. The predictions for binary alloys Al–Mg and Al–Mn are in very good agreement with experiments over a range of concentrations and temperature. The model is not accurate for Al containing very dilute (ppm) Fe. When the anomalous behavior associated with very dilute concentrations of Fe is included, the predictions for Al–Cr–(Fe) and Al–Cu–(Fe) are also in very good agreement with experiment. Predictions of the activation volume, a sensitive test of the thermal activation process, are also in general agreement with experiments and the overall model obeys Basinski’s “stress equivalency” principle [29]. Although the analysis is carried out using Al as the host matrix, the approach is applicable to other metals with substitutional solutes, particularly fcc and hcp systems. The predictive success of the model demonstrates that computational materials science can provide quantitative predictions of material mechanical behavior, including the effects of alloying, opening the path to computational alloy design.

## 2. Computational methods

To make quantitative predictions, it is necessary to accurately determine  $U(\vec{r})$  over a wide range of solute atoms and for all possible solute locations  $\vec{r}$ . In particular, solutes that are immediately above and below the partial dislocations and stacking fault (hereafter called “the core”) are in a local environment much different from the bulk and therefore likely cannot be described by classical continuum elasticity. Accurately calculating the interaction energies of solutes in the core requires the use of a first-principles method to determine both the structure of the core and the energy changes when a solute atom substitutes for a host atom in the core region. Here, we use DFT, implemented using the Vienna Ab-initio Simulation Package (VASP) [30,31], Vanderbilt ultrasoft pseudopotentials [32] and the generalized gradient correction by Perdew and Wang [33,34]. For bulk fcc Al, the method predicts a Burgers vector  $b = 2.86 \text{ \AA}$ , a shear modulus  $\mu = 27.4 \text{ GPa}$  and a stacking fault energy  $\sigma_{\text{sf}} = 124 \text{ mJ m}^{-2}$ , all in good agreement with experiments [35]. The pseudopotential valence configurations (PVC) and plane-wave cutoff (PWCO) energies used for Mn and Fe solutes are as follows: Mn,  $[Ar]d^6 4s^1$ , 295 eV; Fe,  $[Ar]d^7 s^1$ , 238 eV. The PVC and PWCO for Al and all other solutes are summarized in Ref [28]. In calculating the relaxed core structure, a  $2 \times 2 \times 8$  Monkhorst–Pack kmesh [36] and Methfessel–Paxton energy broadening [37] of 1 eV are used.

We first determine the equilibrium geometry of a pure Al  $a/2 \langle 110 \rangle$  edge dislocation with line direction along

the  $\langle 11\bar{2} \rangle$  direction. We use the lattice Green’s function method of Woodward et al. [35,38]. We use a computational cell composed of 569 Al ions forming a prolate ellipse with major and minor axes dimensions of approximately 18 and 14  $\text{\AA}$  within an overall simulation box of dimensions  $61 \times 65 \times 4.95 \text{ \AA}$  and having periodic boundary conditions. Geometry optimizations were conducted until the forces on the ions in region I (the inner 50 atoms) were  $5 \text{ meV \AA}^{-1}$  or less. This ellipsoidal shape differs from the cylindrical shape used in Ref. [35] and provides more freedom for the splitting of the fcc core, and thus a better representation of the core structure than in the previous work. The equilibrium dislocation geometry shown in Fig. 1 has a core dissociated into Shockley partials separated by approximately 10.8  $\text{\AA}$ , slightly larger than the value previously quoted in Ref. [35].

The solute–dislocation interaction energy as a function of solute position is computed by substituting a single solute atom into each of 22 distinct atomic core sites immediately above and below the slip plane. For Mg and Cr, two additional sites in the middle of the core in the second rows above and below the slip plane were also investigated. The structure was then relaxed using DFT-derived forces in region I until the forces on all the ions in region I were  $5 \text{ meV \AA}^{-1}$  or less. The lattice Green’s function optimization was not performed because continuum elasticity and molecular statics using embedded atom method (EAM) potentials for Al–Mg [12] show that the difference in energies is negligible ( $\sim 1 \text{ meV}$ ) and a set of ancillary DFT

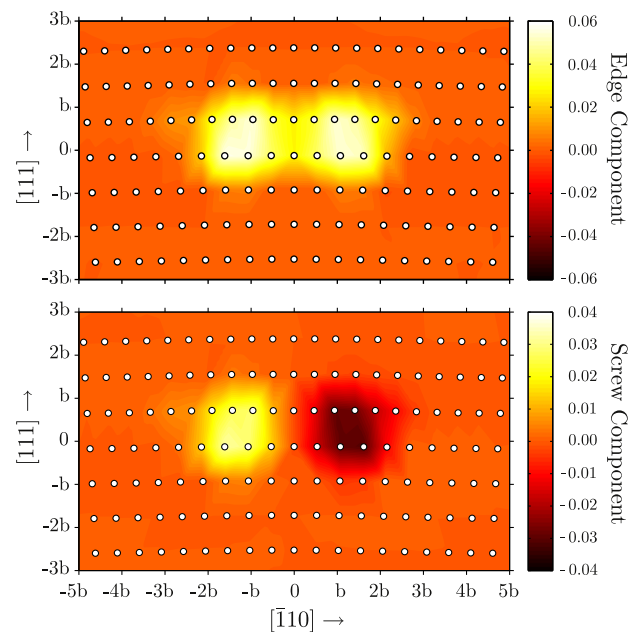


Fig. 1. Nye tensor distribution for the (a) edge and (b) screw components of the Al edge dislocation core computed using DFT and the Lattice Green’s Function method. The  $x$ -axis is in units of Burgers vector  $b = 2.86 \text{ \AA}$ . Peaks in the Nye tensor roughly correspond to the locations of the partial dislocations in the dissociated core.

tests confirmed this conclusion. For magnetic solutes (Cr, Fe and Mn), spin-polarized calculations were performed assuming an initial spin moment of 5  $\mu\text{B}$ . The Fe and Mn solutes retained magnetic moments in all sites explored, while Cr solutes did not.

From the energy  $E_{\text{disl+solute}}(x_i, y_j)$  of the simulation cell containing a dislocation and a solute at  $(x_i, y_j)$ , the interaction energy is computed as

$$U(x_i, y_j) = E_{\text{disl+solute}}(x_i, y_j) - [E_{\text{disl only}} + E_{\text{ref}}] \quad (4)$$

where  $E_{\text{disl only}}$  is the energy of the pure Al core and  $E_{\text{ref}}$  is the energy of a single solute in a bulk fcc Al crystal. Direct calculation of  $E_{\text{ref}}$  using the same simulation cell but containing undeformed fcc Al is not accurate, presumably due to differences in the surfaces effects/energies between the two geometries. For consistency with the core calculations,  $E_{\text{ref}}$  is estimated as the mean of solute energy in the 22 core sites

$$E_{\text{ref}} = \frac{1}{22} \sum_{i,j} (E_{\text{disl+solute}}(x_i, y_j) - E_{\text{disl only}}) \quad (5)$$

Due to asymmetry in the magnitude of the solute energies just above and below the stacking fault, this estimate of  $E_{\text{ref}}$  has some uncertainty, but the uncertainty in the predicted strength is second order in the uncertainty of  $E_{\text{ref}}$  and is small. For instance, in the case of Al–Mg alloys, an uncertainty of as much as 0.05 eV (a very large value) would result in only a 7% change in the predicted strength. Our estimate for  $E_{\text{ref}}$  also has the advantage of filtering out systematic errors in energy that are independent of solute position and further mitigates the boundary effects caused by not relaxing ions outside region I.

The effect of solute–solute interactions along the  $\langle 1\bar{1}2 \rangle$  direction was explored by doubling the periodicity of the simulation cell along the line direction from 4.95 to 9.90 Å, thereby increasing the solute–solute spacing by the same amount. The differences in interaction energies were minimal ( $\approx 6\%$ ), consistent with the EAM results for Al–Mg of Olmsted et al. [12] and with the continuum prediction of zero interaction energy between two separate point dilatational sources [39].

Away from the immediate core region, substitutional solutes are in a local fcc environment that is far less distorted than in the immediate core. Therefore, the continuum approximation of Eq. (1),  $U(x_i, y_j) \approx -p(x_i, y_j)\Delta v_m$ , should provide a good approximation of the interaction energies with increasing distance from the core region. However, the pressure field  $p(x_i, y_j)$  must be that appropriate for the real dissociated core structure. We use a simple approach of spreading the Burgers vector into  $n + 1$  dislocations, each of Burgers vector  $b/(n + 1)$ , evenly spaced by  $b/2$ , over  $n + 1 = 11$  interstitial sites along the slip plane in the core region. The pressure field is then computed as

$$p(x_i, y_j) = -\frac{1 + \nu}{3\pi(1 - \nu)} \mu \frac{b}{n + 1} \sum_{l=-n/2}^{n/2} \frac{y_j}{[x_i - l(\frac{b}{2})]^2 + y_j^2} \quad (6)$$

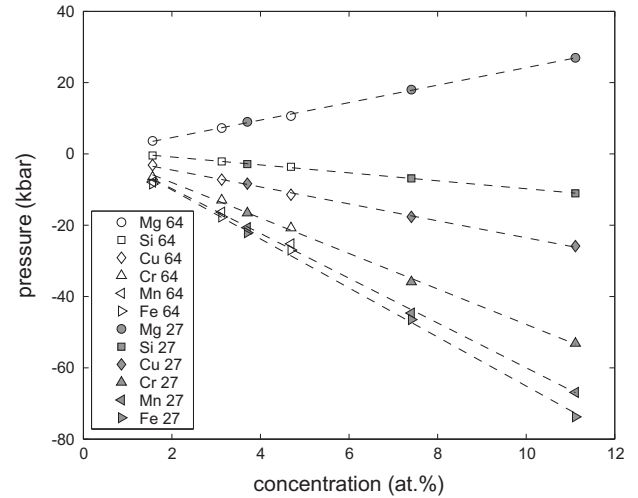


Fig. 2. Pressure vs. concentration in fixed-volume supercells containing solutes atoms, for Mg, Si, Cu, Cr, Mn and Fe solutes, for both 27- and 64-atom supercells. Dashed lines are linear fits using data from both supercells for each solute, and the slopes of these lines are used in Eq. (7) to compute the misfit volume.

where  $\nu$  is the Poisson's ratio of Al. This simple approximation was validated in EAM calculations of Al–Mg by Olmsted et al. [12].

Direct calculation of the misfit volume  $\Delta v_m$  through DFT volume relaxation calculations of perfect Al crystals containing a single solute atom shows inconsistent results between different supercell sizes. To obtain consistent results, we follow the more complex method to calculate  $\Delta v_m$  proposed by Vannarat et al. [40]. Using both 27- and 64-atom supercells, internal geometry optimizations are performed with one, two and three solute atoms, and the change in pressure in these supercells was computed via DFT in VASP. The dependence of the pressure with concentration is very linear for all solutes considered, as shown in Fig. 2, consistent with results in Ref. [40]. The misfit volume is then calculated using the slope of the pressure vs. solute concentration and the DFT-computed bulk modulus  $B$  of pure Al [35],

$$\Delta v_m = \left( \frac{\partial \Delta v_m}{\partial c} \right) c_{1\text{sol}} = \left( \frac{1}{B} \frac{\partial p}{\partial c} \right) c_{1\text{sol}} \quad (7)$$

where  $c_{1\text{sol}}$  is the concentration of one solute in the supercell. The misfit volumes calculated using the two supercells differ by less than 15% across all the solutes considered. The misfit volume is taken as the average of the two derived values, and is shown in Table 1 for all solutes. The uncertainty in  $\Delta v_m$  causes uncertainties of 10% or less in the yield strength predictions.

Using the DFT results in the core and the continuum analytic model outside the core leads to the solute/dislocation energies  $U_{ij} \equiv U(x_i, y_j)$  shown in Fig. 3 for Mg, Si, Cr, Cu, Mn and Fe solutes. Not surprisingly, solutes that are smaller ( $\Delta v_m < 0$ ) than the host Al atom (Si, Cr, Cu, Mn and Fe) tend to be on the compression side of the core,



Table 1

The misfit volume  $\Delta v_m$  for Mg, Cr, Si, Cu, Mn and Fe solutes in Al. Also shown are the predicted  $T = 0$  yield stress  $\tau_{y0}$  and energy barrier  $\Delta E_b$  for each solute. Parameters in bold for Fe solutes are back-calculated from experimental data [43]. Note that all these parameters are different from Ref. [28] due to the use of a more accurate line tension value.

Solute	$\Delta v_m$ ( $\text{\AA}^3$ )	$\tau_{y0}/c^{2/3}$ (MPa)	$\Delta E_b/c^{1/3}$ (eV)
Mg	5.71	342	4.06
Cr	−11.68	705	6.65
Si	−2.65	137	2.58
Cu	−5.57	348	4.10
Mn	−13.31	711	7.53
Fe	−16.44	1072 ( <b>13,238</b> )	8.20 ( <b>28.8</b> )

while those that are larger (Mg) tend to be on the tension side. The interaction energies are generally asymmetric between tension and compression in the layers immediately adjacent to the stacking fault. In most cases, there is a smooth transition between the DFT and the continuum regions, wherein the energies are highest in the immediate core region and decrease steadily with increasing distance from the core. The exceptions to this are Mn and Fe solutes, where the interaction energies in the second row are slightly higher than those in the core. In general, there are no sharp discontinuities in  $U_{ij}$  despite the different methodologies employed in calculating the energies in the two regions, showing the consistency of the two approaches and the accuracy of  $U(x_i, y_j) \approx p(x_i, y_j)\Delta v_m$  just outside the core region.

The first-principles computation of solute/dislocation interaction in the dislocation core is the first main result

of this paper. While a significant computational challenge with various subtleties, the interaction energies by themselves are insufficient to predict strengthening. Thus, in the next section, we develop a detailed model of solute strengthening that uses the interaction energies computed here as input.

### 3. Solute strengthening model

An initially straight dislocation of length  $L$  in a field of randomly distributed solutes can lower its energy by bowing out into regions of the solid containing favorable fluctuations. The lateral length  $\zeta$  of the favorable regions and their typical separation  $w$  along the slip direction must be determined by minimizing the total energy of the dislocation line. To make analytic progress, we simplify the possible dislocation configurations. In this simplified geometry, the dislocation comprises straight segments of length  $\zeta$  lying in favorable local environments separated by roughening amplitude  $w$  along the slip direction, as depicted in Fig. 4. Since it is generally not possible to abruptly transition from one favorable local environment to another, straight segments are connected to each other via additional segments of length  $\zeta$ . For the case of  $w \ll \zeta$ , this geometry is close to a smooth piecewise sinusoidal dislocation configuration. In this geometry, the dislocation can be divided into  $L/2\zeta$  unit cells, each with a segment of length  $\zeta$  lying in an energetically favorable local environment.

The change in total energy as the dislocation moves from the straight configuration to the bowed out configura-

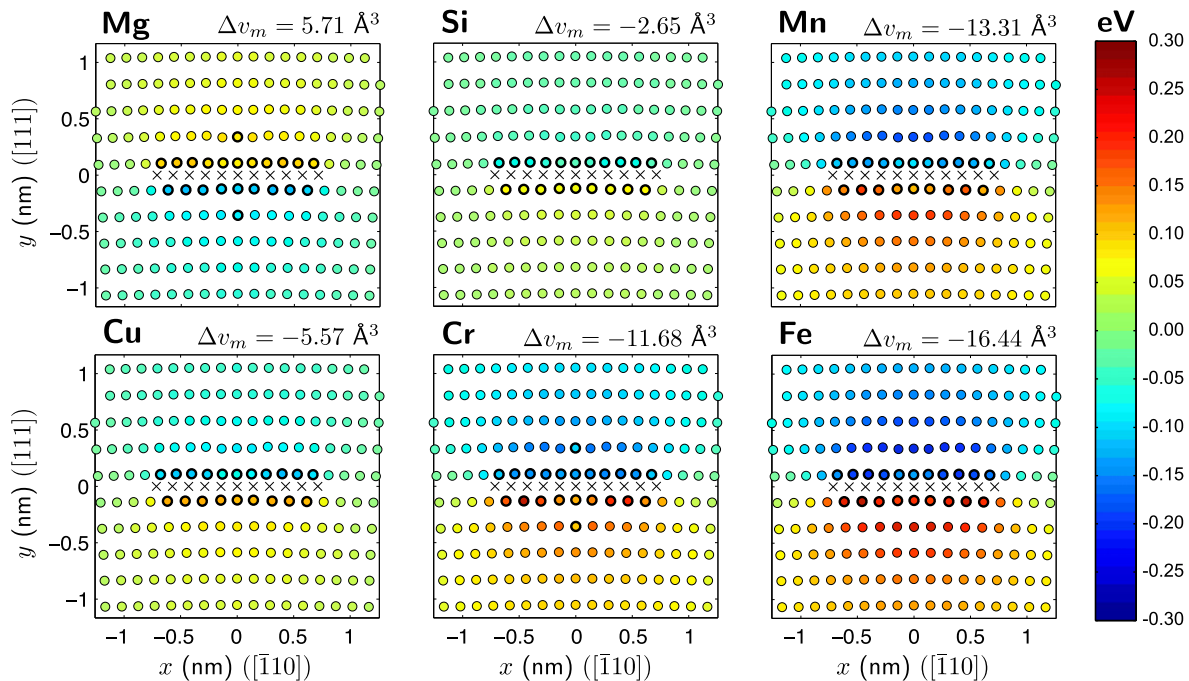


Fig. 3. Solute/dislocation interaction energy  $U_{ij}$  vs. solute position  $(x_i, y_j)$  for Mg, Cr, Si, Cu, Mn and Fe solutes. The misfit volume  $\Delta v_m$  is shown for each solute. Negative energies indicate binding. Bold circles show positions at which first-principles interaction energies are calculated; “x” markers denote positions of the  $b/11$  Burgers vector used to compute the analytic pressure field outside the immediate core sites (non-bold circles).

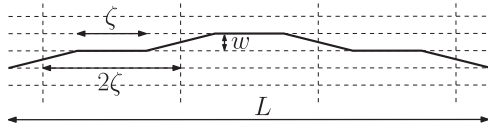


Fig. 4. Schematic of a dislocation roughening into segments of length  $2\zeta$  with roughening amplitude  $w$  due to favorable solute fluctuations.

tion is the sum of the potential energy decrease due to solute/dislocation binding,  $\Delta E_p$ , and the elastic energy increase due to the increase in line length,  $\Delta E_{el}$ ,

$$\Delta E_{tot} = \Delta E_p + \Delta E_{el} \quad (8)$$

For an isotropic line tension model with line tension  $\Gamma$ , the elastic energy is

$$\Delta E_{el} = \Gamma \left[ (\zeta^2 + w^2)^{\frac{1}{2}} - \zeta \right] \cdot \left( \frac{L}{2\zeta} \right) \approx \Gamma \left( \frac{w^2}{2\zeta} \right) \left( \frac{L}{2\zeta} \right) \quad (9)$$

since  $w \ll \zeta$  is expected. Calculation of the binding energy due to solute fluctuations is more subtle, as noted in the introduction, due to divergences that arise when simply summing the energies or fluctuation in energies. However, by recognizing that the total interaction energy as the dislocation segment moves between two positions is correlated over some distance, a finite, calculable solute binding energy and strength emerge naturally without any need to truncate the range of interaction energies, as described below.

Consider a dislocation segment of length  $\zeta$  in a random field of solutes. At each atomic position  $(x_i, y_j)$  projected in the plane normal to the dislocation line, there are  $n_{ij}$  solutes in the length  $\zeta$ , where  $n_{ij}$  is a random number between zero and  $N = \zeta/\sqrt{3}b$  (for a line direction of  $\langle 11\bar{2} \rangle$  in an fcc material). The energy of a segment at the origin is then

$$U_{tot}(\zeta) = \sum_{ij} n_{ij} U_{ij} \quad (10)$$

Moving the dislocation a distance  $w$  from the origin in the slip direction is equivalent to moving the solutes from  $(x_i, y_j)$  to  $(x_i - w, y_j)$  while keeping the dislocation at the origin. The energy change,  $\Delta U_{tot}(\zeta, w)$ , of the dislocation segment of length  $\zeta$  as it glides a distance  $w$  away from the origin can then be expressed as

$$\Delta U_{tot}(\zeta, w) = \sum_{ij} n_{ij} \Delta U_{ij}(w) \quad (11)$$

where  $\Delta U_{ij}(w) = U(x_i - w, y_j) - U(x_i, y_j)$  and the summation in Eq. (11) extends to all in-plane sites. The mean energy change  $\langle \Delta U_{tot}(\zeta, w) \rangle$  vanishes for all values of  $w$  because  $\langle n_{ij} \rangle = cN$  is constant, implying that the configurational force due to solute/dislocation interaction can only arise due to spatial fluctuations in solute concentration. Such fluctuations create a statistical distribution of total energies for a segment characterized by the standard deviation of Eq. (11),

$$\sigma_{\Delta U_{tot}}(\zeta, w) = [\langle \Delta U_{tot}(\zeta, w)^2 \rangle - \langle \Delta U_{tot}(\zeta, w) \rangle^2]^{\frac{1}{2}} \quad (12)$$

Some regions give rise to binding,  $\Delta U_{tot} < 0$ , with characteristic energy  $-\sigma_{\Delta U_{tot}}$ , and others give rise to repulsion,

$\Delta U_{tot} > 0$ , with characteristic energy  $\sigma_{\Delta U_{tot}}$ . Therefore, the characteristic potential energy decrease by allowing the dislocation segment to move into regions in the solid containing favorable solute fluctuations is

$$\Delta E_p = -\sigma_{\Delta U_{tot}} \cdot \frac{L}{2\zeta} \quad (13)$$

The evaluation of Eq. (12) is presented in Appendix A.

The total average binding energy of a dislocation due to solute/dislocation interaction is then obtained by incorporating Eq. (A.6) into Eq. (13). For low concentrations  $c \ll 1$ ,

$$\Delta E_p(\zeta, w) = - \left[ \left( \frac{c\zeta}{\sqrt{3}b} \right)^{\frac{1}{2}} \Delta \tilde{E}_p(w) \right] \cdot \left( \frac{L}{2\zeta} \right) \quad (14)$$

where

$$\Delta \tilde{E}_p(w) = \left[ 2 \sum_{ij} (1 - \chi(w, y_j)) U(x_i, y_j)^2 \right]^{\frac{1}{2}} \quad (15)$$

and

$$\chi(w, y_j) = \frac{\sum_k U(x_k - w, y_j) U(x_k, y_j)}{\sum_k U(x_k, y_j)^2} \quad (16)$$

is the correlation function between the interaction energies of a solute at  $y_j$  before  $(x_i)$  and after  $(x_i - w)$  the dislocation glides  $w$  away from its original position. For any finite  $w$ ,  $\chi(w, y_j)$  increases as  $|y_j|$  increases, i.e. the interaction energies of a solute far from the dislocation are highly correlated,  $\chi(w, y_j) \rightarrow 1$ , as shown in Fig. 5. Such solutes therefore do not contribute significantly to the change in total energy. The quantity  $\Delta \tilde{E}_p(w)$  is thus finite and there is no need to introduce any artificial truncation in the range of the solute/dislocation interactions.

Incorporating Eqs. (9) and (14) into Eq. (8) gives the total energy change as a function of  $\zeta$  and  $w$ , for a dislocation taking on the configuration depicted in Fig. 4, as

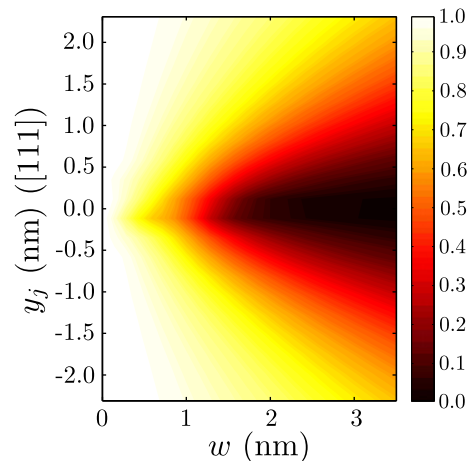


Fig. 5. Energy correlation function  $\chi(w, y_j)$  for a solute initially at  $(0, y_j)$  as the dislocation moves a distance  $w$ , as computed for an Al–Cr alloy.

$$\Delta E_{tot}(\zeta, w) = \left[ \left( \Gamma \frac{w^2}{2\zeta} \right) - \left( \frac{c\zeta}{\sqrt{3}b} \right)^{\frac{1}{3}} \Delta \tilde{E}_p(w) \right] \cdot \left( \frac{L}{2\zeta} \right) \quad (17)$$

To obtain the equilibrium configuration of the dislocation, we minimize Eq. (17) with respect to  $\zeta$  and  $w$ . Analytic minimization with respect to  $\zeta$  is straightforward, yielding the characteristic segment  $\zeta_c$  as a function of the roughening amplitude  $w$  given by

$$\zeta_c(w) = \left( 4\sqrt{3} \frac{\Gamma^2 w^4 b}{c \Delta \tilde{E}_p^2(w)} \right)^{\frac{1}{3}} \quad (18)$$

Incorporating this expression into Eq. (17), the total energy is now solely a function of the roughening amplitude  $w$

$$\Delta E_{tot}(w, \zeta_c(w)) = - \frac{3^{2/3}}{8 \cdot 2^{1/3}} \left( \frac{c^2 \Delta \tilde{E}_p^4(w)}{b^2 w^2 \Gamma} \right)^{\frac{1}{3}} L \quad (19)$$

Minimizing  $\Delta E_{tot}(w, \zeta_c(w))$  with respect to  $w$  yields the equilibrium energy and a characteristic amplitude  $w_c$ . This minimization cannot be done analytically, so it must be done numerically. Scaling out the concentration, the total energy per unit length  $\Delta E_{tot}/Lc^{2/3}$  vs.  $w$  is shown in Fig. 6 for Cr solutes. Fig. 6 also shows the convergence of  $\Delta E_{tot}/Lc^{2/3}$  as a function of the upper limit of the summation over  $y_j$ , which demonstrates that: (i) the characteristic value  $w_c$  is established quite well by the core sites only ( $y_1$  and  $y_{-1}$ ); (ii) the sum converges quickly with increasing number of layers of sites (increasing  $j$ ); and (iii) the magnitude of the contributions from sites within the core ( $y_1, y_{-1}$ ) and outside the core ( $y_j, |j| > 1$ ) are approximately equal, with significant contributions for  $|j| = 2, 3$ . Point (i) above demonstrates that the core structure is crucial for obtaining  $w_c$ , justifying the computational expense of DFT in this

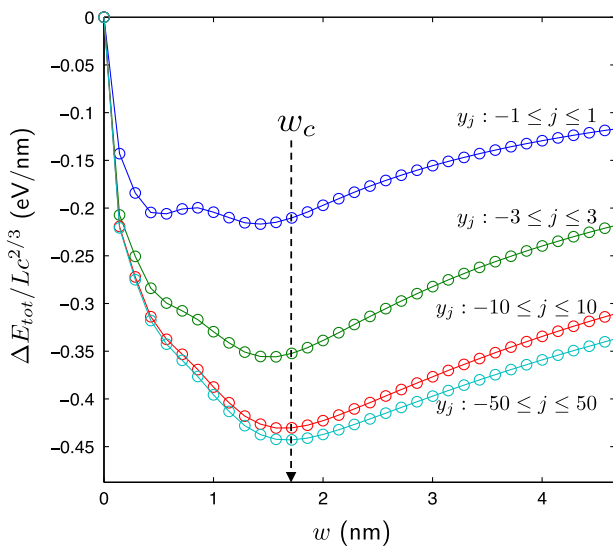


Fig. 6. Normalized total energy per unit length  $\Delta E_{tot}/L c^{2/3}$  vs. roughening amplitude  $w$  for an Al–Cr alloy, for various partial sums over solute sites  $y_j$ , demonstrating the dominance of the core region  $y_{-1}, y_1$  and convergence of the total energy with increasing range of  $|y_j|$ .

region, but point (iii) shows that the region outside the core is also crucial for obtaining an accurate total energy. Calculations for other solutes yield the same general conclusions but with  $w_c$  varying slightly (1.57 nm for Mg, Si and Cu; 1.71 nm for Cr and Fe; and 1.86 nm for Mn) in spite of a large range of misfit volumes among these solutes. The values of  $w_c$  are approximately equal to 1.5 times the core width, so that, when the dislocation moves by  $w_c$ , it encounters a new set of solutes in the core that create a binding energy that is statistically uncorrelated with the energy at the prior position.

After minimization, we have a final total energy per unit length of  $\Delta E_{tot}(w_c, \zeta_c(w_c))/L$ . The relevant characteristic energy is the energy associated with each pinned segment of length  $\zeta_c$  and the surrounding length of  $\zeta_c$  (see Fig. 4), which, from Eqs. (18) and (19), is thus

$$\Delta E_c = \Delta E_{tot}(w_c, \zeta_c(w_c)) \frac{2\zeta_c}{L} = - \frac{3^{5/6}}{2^{5/3}} \left( \frac{c w_c^2 \Gamma \Delta \tilde{E}_p^2(w_c)}{b} \right)^{\frac{1}{3}} \quad (20)$$

Although  $\Delta E_c$  is the characteristic energy, it is not the energy barrier for determining thermally activated motion of the dislocation.  $\Delta E_c$  is the typical energy change on moving from one *arbitrary* point to another point  $w_c$  away. The dislocation is pinned in a local minimum and must escape over the adjacent local maximum, in an energy landscape with a characteristic energy  $\Delta E_c$ . Thus, the energy barrier  $\Delta E_b$  is typically larger than  $\Delta E_c$ , and is determined as follows. First we note that the elastic energy contribution to  $\Delta E_b$  is the same as to  $\Delta E_c$ . We thus concentrate on the potential energy contribution  $\Delta E_p$  to  $\Delta E_b$ . The potential energy landscape, i.e. the energy vs. dislocation position ( $x, y = 0$ ) along the glide plane of the dislocation segment of length  $\zeta_c$ , can be approximated locally as a sinusoid with some amplitude  $\Delta E'_b$ , i.e.

$$E(x) = \frac{\Delta E'_b}{2} \left[ 1 - \cos \left( \frac{\pi x}{w_c} \right) \right] \quad (21)$$

where  $\Delta E'_b$  is the potential energy barrier. From our discussion above,  $\Delta E_p$  is the standard deviation of the change in energy of the dislocation segment as it moves  $w_c$  away,

$$\Delta E_p = \left[ \frac{1}{2w_c} \int_0^{2w_c} (E(x - w_c) - E(x))^2 dx \right]^{\frac{1}{2}} = \frac{1}{\sqrt{2}} \Delta E'_b \quad (22)$$

Thus, the typical potential energy barrier  $\Delta E'_b$  is  $\sqrt{2}$  times larger than  $\Delta E_p$ . We have validated this result via direct stochastic simulations not reported here. The total energy barrier includes the elastic energy contribution, and so is given by

$$\Delta E_b = \Delta E'_b - \Delta E_{el} = \left( \frac{4\sqrt{2} - 1}{3} \cdot \frac{3^{5/6}}{2^{5/3}} \right) \left( \frac{c w_c^2 \Gamma \Delta \tilde{E}_p^2(w_c)}{b} \right)^{\frac{1}{3}} \quad (23)$$

The sign convention in Eq. (23) is the opposite of that in Eq. (20) because the latter refers to the energy change due to the bowing out process while the former refers to the magnitude of the energy barrier.

We have determined that dislocation segments of length  $\zeta_c$  (Eq. (18)) are pinned in typical energy minima with barriers of height  $\Delta E_b$  (Eq. (23)) over a length  $w_c$  (e.g. Fig. 6). We can now use standard analyses of thermally activated dislocation motion to determine the finite- $T$  and rate-dependent yield stress, as follows. When the material is subjected to an applied resolved shear stress  $\tau$ , the energy landscape  $E(\tau, x)$  must be modified to include the work done by the applied stress, and so becomes

$$E(\tau, x) = \frac{\Delta E_b}{2} \left[ 1 - \cos \left( \frac{\pi x}{w_c} \right) \right] - \tau \zeta_c b x \quad (24)$$

The stress-dependent barrier height  $\Delta E(\tau)$  can be approximated (within 6%) by [41]

$$\Delta E(\tau) \approx \Delta E_b \left[ 1 - \left( \frac{\tau}{\tau_{y0}} \right) \right]^{\frac{2}{3}} \quad (25)$$

Here,  $\tau_{y0}$  is the zero-temperature yield strength, i.e. the stress at which the energy landscape exhibits no barrier for dislocation motion

$$\tau_{y0} = \frac{\pi}{2} \frac{\Delta E_b}{b \zeta_c(w_c) w_c} = 1.01 \left( \frac{c^2 \Delta \tilde{E}_p^4(w_c)}{\Gamma b^5 w_c^5} \right)^{\frac{1}{4}} \quad (26)$$

with  $1.01 = \pi(4\sqrt{2} - 1)/3^{1/3} 2^{10/3}$  a constant containing all the numerical factors. At finite temperature, the dislocation can be thermally activated over the barrier at stresses below  $\tau_{y0}$ . For a quasistatic loading, the rate of escape  $v$  by activation over the stress-dependent barrier height  $\Delta E(\tau)$  can be approximated using transition state theory [41] as  $v = v_0 \exp(-\Delta E(\tau)/kT)$ , where  $v_0$  is the attempt frequency,  $T$  is the temperature and  $k$  is Boltzmann's constant. The microscopic dislocation escape rate  $v$  can be related to the macroscopic strain rate  $\dot{\epsilon}$  by the well-established model of Kocks et al. [4], that is  $\dot{\epsilon} = \dot{\epsilon}_0 \exp(-\Delta E(\tau)/kT)$ , where  $\dot{\epsilon}_0 = \rho b d v_0$  is the reference strain rate,  $\rho$  is the dislocation density per unit area and  $d$  is the flight distance over which the dislocation moves after each escape. This relation, along with Eq. (25), can be inverted to obtain the finite temperature stress required for dislocation flow as

$$\tau_y(T) = \tau_{y0} \left[ 1 - \left( \frac{kT}{\Delta E_b} \ln \frac{\dot{\epsilon}_0}{\dot{\epsilon}} \right)^{\frac{3}{2}} \right] \quad (27)$$

Eq. (27) applies at low  $T$  but not at cryogenic  $T$ , where dynamic effects can enter [41]. At high  $T$ , Labusch has shown that the characteristic length  $\zeta_c$  effectively increases as the dislocation can explore other configurations, but with the behavior still controlled by the energy barrier  $\Delta E_b$  [10,42]. Over a wide range of temperature,  $0.2 < kT \ln(\dot{\epsilon}_0/\dot{\epsilon})/\Delta E_b < 0.6$ , this result of Labusch can be matched to Eq. (27) as

$$\tau_y(T) = \tau_{y0} \exp \left( -\frac{1}{0.51} \frac{kT}{\Delta E_b} \ln \frac{\dot{\epsilon}_0}{\dot{\epsilon}} \right) \quad (28)$$

where the parameter 0.51 provides a good fit (<7%) to both Eq. (27) and its derivative with respect to  $T$ . While nearly

identical over a range of temperature, Eq. (28) does not reach zero at any finite temperature, and is thus more accurate at elevated temperatures. Eqs. (23), (26), (27) and (28) are the second main results of this paper.

Associated with thermally activated flow is the activation volume  $V = -\partial \Delta E / \partial \tau$ , which is the area swept out by the dislocation during the activation process multiplied by the Burgers vector. Taking the derivative of Eq. (25) with respect to  $\tau$  yields

$$V(T) = -\frac{\partial \Delta E(\tau)}{\partial \tau} = \frac{3}{2} \frac{\Delta E_b}{\tau_{y0}} \left( \frac{kT}{\Delta E_b} \ln \frac{\dot{\epsilon}_0}{\dot{\epsilon}} \right)^{\frac{1}{2}} \quad (29)$$

Experimentally, a direct relationship between  $V$  and the finite temperature yield stress  $\tau_y$  has been observed, leading Basinski to postulate the so-called “stress equivalency principle”: if two different alloys have the same  $\tau_y$  at the same temperature  $T$  and strain rate  $\dot{\epsilon}$ , then they will also have the same  $V$ , regardless of the concentrations and types of solutes in the two different alloys [29]. “Stress equivalency” is satisfied by the present model under some weak constraints. Specifically, if the roughening amplitude  $w_c$  varies only slightly with the type of solute in the alloy, then the parameter  $c \Delta \tilde{E}_p^2$  controls the values of both  $\tau_{y0}$  and  $\Delta E_b$ , which in turn govern both  $V$  and  $\tau_y$ . Eq. (27) can then be rewritten as a function of  $V$

$$\tau_y = 2.23 \left( \frac{b k T w_c^3 \Gamma \eta}{V^3} \right)^{\frac{1}{2}} \left[ 1 - 0.67 \left( \frac{k T \eta}{\left( \frac{b^3 k T w_c^3 \Gamma^3 \eta}{V^3} \right)^{\frac{1}{2}}} \right)^{\frac{2}{3}} \right] \quad (30)$$

where  $\eta = \ln(\dot{\epsilon}_0/\dot{\epsilon})$ . The activation volume  $V$  and the finite temperature flow stress  $\tau_y$  are thus related by an equation of the form  $\tau_y = A V^{-3/2} (1 - B V^{1/2})$ , where  $A$  and  $B$  are constants. If  $B V^{1/2} \ll 1$ , then  $V$  and  $\tau_y$  are related by a simple power law,  $V \sim \tau_y^{-2/3}$ , which was previously derived for the Labusch model by Nabarro [9]. For different solutes with the same  $w_c$ , Basinski's stress equivalency principle is thus strictly obeyed. Slight variations in  $w_c$  will be manifested as slight rigid shifts preserving the functional form; for all materials studied in this paper, these shifts are small. The activation volume is also predicted to scale as  $c^{-4/9}$ , which is close to the  $\sim c^{-1/2}$  trend reported in the literature [43].

The present model is easily generalized to consider more than one solute. For an arbitrary number of random non-interacting solutes, Eq. (10) is replaced by

$$\Delta U_{tot}(\zeta, w) = \sum_{ij} \left( n_{ij}^{(1)} \Delta U_{ij}^{(1)}(w) + n_{ij}^{(2)} \Delta U_{ij}^{(2)}(w) + n_{ij}^{(3)} \Delta U_{ij}^{(3)}(w) \dots \right) \quad (31)$$

where the superscripts indicate the type of solutes. For the multisolute case, the analysis above then applies with  $c \Delta \tilde{E}_p^2$  replaced by  $\sum_i c_i \Delta \tilde{E}_p^{(i)2}$ . For solutes with the same  $w_c$ , the zero-temperature strength and characteristic energy barrier are

$$\tau_{y0} = \left[ \sum_i \left( \tau_{y0}^{(i)} \right)^{\frac{2}{3}} \right]^{\frac{3}{2}}, \quad \Delta E_b = \left[ \sum_i \left( \Delta E_b^{(i)} \right)^3 \right]^{\frac{1}{3}} \quad (32)$$



The former is consistent with Labusch's analysis [5,7]. Numerical minimization must be used for solutes with different  $w_c$  to determine the effective  $w_c$ , but the difference between direct minimization and Eq. (32) is small for all of the solutes considered in this paper. For instance, the differences in  $\tau_{y0}$  and  $\Delta E_b$  between numerical minimization and Eq. (32) for a 1% Mg ( $w_c = 1.57$  nm)/1% Mn ( $w_c = 1.86$  nm) alloy are 5% and 4%, respectively.

The theory presented in this section utilizes the fundamental solute/dislocation energies as input into a detailed model that culminates in the prediction of the characteristic energy barrier and length scales for dislocation motion through the material. Use of first-principles data overcomes the problem of lack of knowledge of solute interactions in the core of the dislocation. Careful analysis of the correlations in solute fluctuations overcomes the apparent problem of diverging energies that inhibited earlier approaches from being parameter free. From these fundamental properties, the finite- $T$ , rate-dependent yield stress follows naturally via thermal activation theory, with no adjustable parameters at any stage. The model is related conceptually to the classic Labusch model, predicting similar scalings with concentration and stress equivalency, and generalized to multiple solute types, but has succeeded in eliminating ad hoc features and the fitting of parameters used in prior implementations of the Labusch concepts. We next turn to predictions of the model when applied to Al–X alloys to demonstrate the quantitative predictability of the model.

#### 4. Results and discussion

Using the interaction energies calculated in Section 2 and the strengthening model presented in Section 3, the zero temperature stress scaled by concentration,  $\tau_{y0}/c^{2/3}$ , and the energy barrier scaled by concentration,  $\Delta E_b/c^{1/3}$ , are presented in Table 1 for Mg, Si, Cu, Cr, Mn and Fe solutes in Al. The line tension used,  $\Gamma = 0.47$  eV Å<sup>−1</sup>, is based on new robust molecular statics calculations on EAM Al [44]. The quoted values in Table 1 have an estimated uncertainty of 5–10% due to uncertainties in the reference interaction energy,  $E_{\text{ref}}$ , and the computed misfit volumes,  $\Delta v_m$ . Using Eqs. (32) and (27), the finite temperature flow stress of an alloy containing any number of these solutes can be predicted, with no parameters. Modifications to the detailed analysis in Section 3, such as consideration of a different geometry to that depicted in Fig. 4, would lead only to a shift by an overall constant factor independent of solute type or concentration.

The experimental flow stress values of 12 distinct and well-characterized Al–X alloys have been measured at 78 K and  $\dot{\epsilon} = 3 \times 10^{-5}$  s<sup>−1</sup> by Diak et al. [43,45,46]. Values for  $\dot{\epsilon}_0$  typically range from  $10^4$  to  $10^6$  s<sup>−1</sup>; appearing in a logarithm, the precise value is not crucial and we use  $10^4$  s<sup>−1</sup>. The flow stresses are measured using a 0.02% strain offset, corresponding to the onset of plastic flow associated with dislocation motion in tension tests on polycrystalline

materials. The predicted shear flow stresses must therefore be multiplied by the Taylor factor  $M = 3$  in order to compare with experiments.

Table 2 shows the predicted and experimental flow stresses for all nominally binary Al–X alloys. Predictions for the Al–Mg alloys are in very good agreement with experimental values, being only ~15% lower. Predictions for the Al–Mn alloys are similarly close to the experimental values. In contrast, the Al–Fe alloys containing parts per million (ppm) of Fe solutes are drastically underestimated, with predictions of virtually zero strength and experiments showing strengths on the order of tens of megapascals. It is clear that the strengthening due to dilute Fe solutes cannot be explained by the interaction energies calculated in Section 2 and the model of Section 3. This may be due to directional bonding between the Fe and Al atoms within the dislocation core. The predicted strengths for the Al–Cr and Al–Cu alloys are somewhat smaller than those found in experiments, although the general trends are captured. For instance, the Al–Cu and Al–Cr alloys with similar solute concentrations have strengths differing by a factor of approximately two in both predictions and experiments. The difference between theory and experiment for these two alloys lies in the presence of ppm Fe in these nominally binary alloys.

It is beyond the scope of this paper to address the Al–Fe system in more detail; this will be done in a subsequent publication. We can, however, account for the role of Fe in the nominally binary Al–Cr–(Fe) and Al–Cu–(Fe) alloys using the experimental results for Al–Fe, as follows. The experimental yield stresses for Al–Fe scale reasonably well with  $c^{2/3}$ , suggesting that Labusch scaling applies to the Fe solutes despite the anomalous magnitude. We thus use the experimental yield stresses at  $T = 78$  K to back-calculate an effective value for  $c\Delta E_p^2$  for Al–Fe, from which we then obtain experimentally derived values of  $\tau_y/c^{2/3} = 13,238$  MPa and  $\Delta E_b/c^{1/3} = 28.8$  eV. Predictions for the Al–Cr–(Fe) and Al–Cu–(Fe) alloys using the theory plus the

Table 2

Predicted and experimental [43,45] tensile yield stresses at  $T = 78$  K for various Al–X alloys. Solute concentrations are from Diak et al. [43,45]. Predictions in bold use experimentally derived parameters for Fe. Note that these results are different from Ref. [28] due to the use of a more accurate line tension value.

Solute	$c$ (%)	Tensile yield stress $\sigma_y$ (MPa)	
		Predicted (78 K)	Experiment (78 K)
Mg	0.444	18.2	20.6
Mg	0.810	28.9	34.2
Mn	0.123	17.1	20.8
Mn	0.246	28.8	28.9
Mn	0.494	48.1	44.0
Fe	$7.7 \times 10^{-4}$	0.1	11.0
Fe	$16.9 \times 10^{-4}$	0.5	16.7
Fe	$43.5 \times 10^{-4}$	1.6	33.4
Cr–(Fe)	$0.073 (10 \times 10^{-4})$	11.0 ( <b>19.4</b> )	23.7
Cr–(Fe)	$0.302 (12 \times 10^{-4})$	32.5 ( <b>38.8</b> )	50.2
Cu–(Fe)	$0.090 (12 \times 10^{-4})$	5.3 ( <b>16.7</b> )	12.3
Cu–(Fe)	$1.650 (50 \times 10^{-4})$	51.1 ( <b>75.8</b> )	86.6

experimentally derived parameters for Fe are shown in Table 2 (in bold text) with Eq. (32), and good agreement with experiments is now obtained for all cases.

Fig. 7 shows the experimental yield stress vs. the predicted value for all of the alloys except Al–Fe, graphically demonstrating consistent agreement across the entire range of alloys at  $T = 78$  K. Diak et al. have also recently measured the yield stresses of Al–Mn alloys at several elevated temperatures [46]. Using the parameters in Table 1 and the theory of Eq. (28), predictions for Al–Mn at all three temperatures are included in Fig. 7. The agreement is again very good over the entire range of data.

Diak and colleagues measured the activation volumes of the Al–Mn alloys at 78 K [43,45]. Fig. 8 shows the activation volume  $MV/b^3$  vs. the  $T = 78$  K shear yield stress  $\tau_y = \sigma_y/M$ , where  $M = 3$  is the Taylor factor, in log–log form to elucidate any power-law scaling and stress equivalency. The predicted  $V$  are of the same magnitude as the experimentally measured values, but typically over-estimate the experiments by roughly a factor of two. We consider this parameter-free prediction to be in good agreement with experiments because the activation volume reflects the product  $b\zeta_c w_c$  that involves the two key length scales emerging from the theory. The predicted values fall nearly along a single curve, reflecting the stress-equivalency principle with the small variations attributable to differences in  $w_c$  among alloys. Both experiments and predictions are approximately linear, indicating power-law scaling, but the slopes indicate two different power laws:  $V \sim \tau_y^{-0.6}$  is predicted, while the experimental trend is  $V \sim \tau_y^{-1.0}$ . One possible source of the discrepancy between the experimental and predicted activation volumes is associated with the value of the line tension  $\Gamma$ . The finite

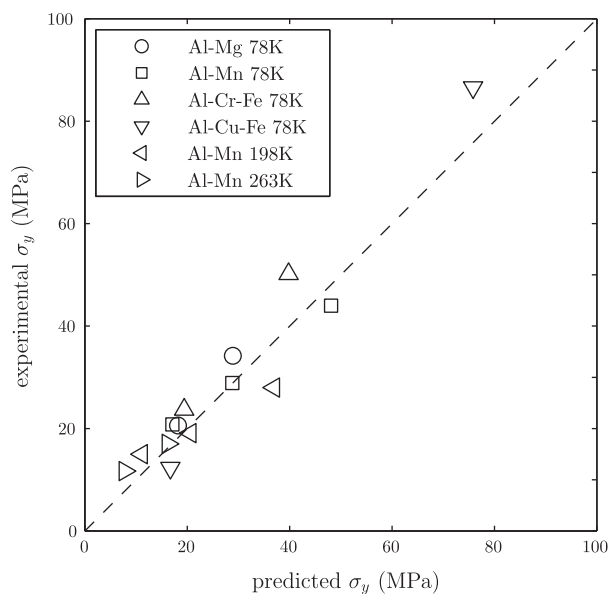


Fig. 7. Experimental [43,45,46] vs. predicted flow stress  $\sigma_y$  for nine distinct alloys at various temperatures, showing overall good agreement. The dashed line has a slope of unity and indicates perfect agreement.

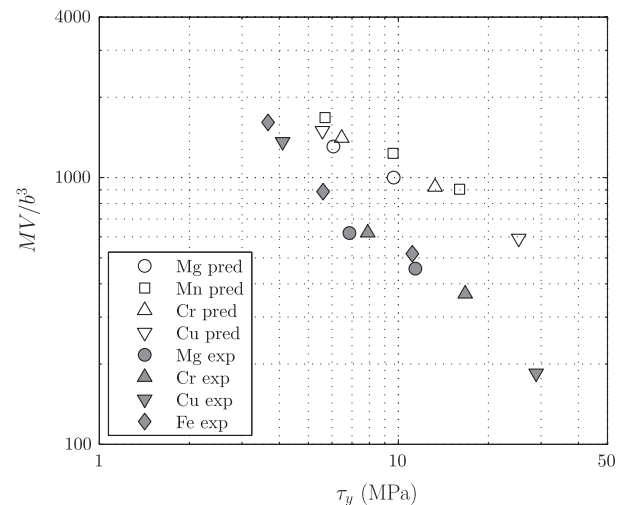


Fig. 8. Normalized activation volume  $MV/b^3$  vs. 78 K shear yield stress  $\tau_y$  for both experimental [43] and predicted results, in log–log form, demonstrating stress equivalency.

temperature stress  $\tau_y(T)$  is only weakly dependent on  $\Gamma$  because the zero temperature yield stress scales as  $\Gamma^{-1/3}$  and the energy barrier scales as  $\Gamma^{1/3}$ , and these opposite dependencies on  $\Gamma$  partially cancel each other out. However, the activation volume depends on the ratio of these quantities, and scales as  $\Gamma^{5/9}$ . A line tension  $\Gamma$  smaller than the EAM Al-derived value of  $\Gamma = 0.47$  eV would decrease the predicted activation volumes by a constant factor, with a somewhat smaller decrease in predicted yield stress. Additionally, non-solute-related strengthening mechanisms, such as a Peierls barrier, can influence the slope of the experimentally measured  $V$  without having too much effect on the yield stress itself. Overall, reasonable agreement in the values for  $V$  supports the model presented here.

## 5. Final remarks

We have shown that first-principles calculations of the interaction energy coupled with a parameter-free solute strengthening model leads to predicted flow stresses that agree with experiments over a wide range of Al alloys. The model both resolves fundamental difficulties encountered in existing literature models and avoids introducing any adjustable parameters. Previous predictions using first-principles input were limited to zero-temperature flow stresses and provided little insight into the temperature and strain-rate dependence of the strengthening.

While the results are promising, the model only applies to moderate solute concentrations where Mott/Labusch statistics [47] apply. For extremely dilute concentrations, Friedel statistics [48] govern the strengthening behavior of solutes, and a point pinning model such as the one presented in Ref. [25] may be more applicable. It is therefore important to better understand the transition between these two regimes. Previous literature has explored this transition [7,13,47–49], but a quantitative determination of the

transition is yet to be achieved. Possibly related to this issue is the anomalous behavior of dilute Fe in Al. The high strengthening of Fe, relative to predictions here and all other solute additions, has implications for alloy design and processing, so must be better understood.

In the absence of first-principles input, e.g. for other solutes or other host materials than those studied here, the analytic model here can be treated as a two-parameter model in terms of the zero-temperature flow stress  $\tau_{y0}$  (Eq. (26)) and the energy barrier  $\Delta E_b$  (Eq. (23)), which is generic to thermal activation theory. More subtle is the fact that  $\tau_{y0}$  and  $\Delta E_b$  depend on the fundamental parameters  $c\Delta\tilde{E}_p^2$  and  $w_c$ . If  $w_c$  is taken as 1.5 times the core width for a given host, then the model here reduces to a one-parameter theory. Experimental data can then be compared to predictions in which  $c\Delta\tilde{E}_p^2$  is used to fit temperature- and/or concentration-dependent data.

An alternative simple approach also emerges by interpreting our results from a pure continuum elasticity perspective. While formally inadequate in the core, continuum elasticity suggests that  $\Delta\tilde{E}_p \sim \Delta v_m$  [39], and thus that  $\tau_{y0} \sim \Delta v_m^{4/3}$  and  $\Delta E_b \sim \Delta v_m^{2/3}$ . Our full first-principles data, culminating in the results of Table 1, follows this scaling fairly closely:

$$\tau_{y0}/c^{2/3} \approx (31.1 \pm 6.3 \text{ MPa}/\text{\AA}^{-14})\Delta v_m^{4/3} \quad (33)$$

$$\Delta E_b/c^{1/3} \approx (1.31 \pm 0.03 \text{ eV}/\text{\AA}^{-12})\Delta v_m^{2/3} \quad (34)$$

Thus, it may be possible to use inexpensive first-principles methods to compute the surrogate material parameter  $\Delta v_m$ . For new host matrix materials, the coefficients above would be unknown, but fitting to limited experimental data on one solute might reveal the coefficients, which would then permit application to other solutes or combinations of solutes. However, the variations in Eq. (34) suggest that such an approach has limited accuracy, with predictions of the zero-temperature strength deviating by up to  $\pm 30\%$ . With smaller variations in the energy barrier, the finite- $T$  strength would thus deviate by a similar  $\pm 30\%$ . The full predictions here are generally in much better agreement with experiment, although requiring far greater computational cost. Such a strategy is similar in spirit to the work of Zander et al. [26,27], who computed  $\Delta v_m^{(i)}$  for various solutes using first-principles and then assumed  $\sigma_y = K \sum_i c_i^{2/3} \Delta v_m^{(i)4/3}$ , with  $K$  as a single fitting parameter independent of solute. However, our analysis here shows that the additivity assumed by Zander et al. should be replaced by Eq. (32). We also provide additional insight into the energy barrier so that the results can be applied at finite temperature, although Eq. (34) shows such an approach to have only reasonable accuracy.

The overall methodology presented here is robust and can readily be applied to other fcc alloys as well as basal slip in hcp alloys. We will report on the application of the model to basal slip in Mg–Al in a forthcoming paper. This model thus represents a significant advance in computational metallurgy that can be used to guide the design of technologically important multicomponent solute-strengthened alloys.

## Acknowledgements

The authors thank B.J. Diak and D. Warner for helpful discussions. Support for this work was provided through the GM/Brown Collaborative Research Laboratory on Computational Materials Research, with additional support through the NSF Materials Research Science and Engineering Center at Brown on Micro- and Nano-Mechanics of Materials (Grant DMR-0520651).

## Appendix A. Derivation of average solute energy fluctuation

$\sigma_{U_{tot}}$

To evaluate Eq. (12), we first express the first term on the right-hand side of the equation as

$$\begin{aligned} \langle \Delta U_{tot}(\zeta, w)^2 \rangle &= \sum_{ij} \langle n_{ij}^2 \rangle \Delta U_{ij}(w)^2 + \sum_{ij} \sum_{lm \neq ij} \langle n_{ij} \rangle \\ &\quad \times \langle n_{lm} \rangle \Delta U_{ij}(w) \Delta U_{lm}(w) \end{aligned} \quad (A.1)$$

since  $n_{ij}$  is the only random variable in the equation. The quantity  $\langle n_{ij}^2 \rangle$  is given by the binomial theorem as

$$\langle n_{ij}^2 \rangle = \sum_{n=0}^N \frac{N!}{n!(N-n)!} p^n q^{1-p} n^2 \quad (A.2)$$

where  $p$  is the probability of finding a solute at position  $(x_i, y_j)$ , which, for random solutes, is independent of position, and  $q = 1 - p$ . Noting that  $n^2 c^n = (p \cdot \partial/\partial p)^2 (p^n)$ ,  $n_{ij} \leq N$  and  $p = c$ , Eq. (A.2) reduces to

$$\langle n^2 \rangle = (cN)^2 + Nc(1-c) = \langle n \rangle^2 + c(1-c)N \quad (A.3)$$

Incorporating Eq. (A.3) into Eq. (A.1) yields

$$\begin{aligned} \langle \Delta U_{tot}(\zeta, w)^2 \rangle &= \left[ \langle n \rangle^2 + c(1-c)N \right] \sum_{ij} \Delta U_{ij}(w)^2 \\ &\quad + \langle n \rangle^2 \sum_{ij} \sum_{lm \neq ij} \Delta U_{ij}(w) \Delta U_{lm}(w), \end{aligned} \quad (A.4)$$

$$= c(1-c)N \sum_{ij} \Delta U_{ij}(w)^2 + \langle \Delta U_{tot}(\zeta, w) \rangle^2 \quad (A.5)$$

Incorporating Eq. (A.4) into Eq. (12) gives the expected fluctuation in the interaction energy when a segment of length  $\zeta$  moves a distance  $w$  as

$$\sigma_{\Delta U_{tot}}(\zeta, w) = c(1-c)N \sum_{ij} \Delta U_{ij}(w)^2 \quad (A.6)$$

## References

- [1] Fleischer R.L. Acta Metall 1961;9:996–1000.
- [2] Fleischer R.L. Acta Metall 1963;11:203–9.
- [3] Haasen P, Mordike BL. Physical Metallurgy. 3rd ed. Cambridge: Cambridge University Press; 1996.
- [4] Kocks UF, Argon AS, Ashby MF. Prog Mater Sci 1975;19:1–281.
- [5] Labusch R. Phys Status Solidi B 1970;41:659–69.
- [6] N.F. Mott, F.R.N. Nabarro, in: Physical Society of Bristol Conference Report, 1948, pp. 1–19.
- [7] Labusch R. Acta Metall 1972;20:917–27.
- [8] Nabarro FRN. Proc Roy Soc Lond, Ser A 1985;381:285–92.
- [9] Nabarro FRN. Philos Mag B 1985;52:785–93.

- [10] Zaiser M. *Philos Mag A* 2002;82:2869–83.
- [11] Nixon WE, Mitchell JW. *Proc Roy Soc Lond, Ser A* 1981;376:343–59.
- [12] Olmsted DL, Hector Jr LG, Curtin WA. *J Mech Phys Solids* 2006;54:1763–88.
- [13] Schwarz RB, Labusch R. *J Appl Phys* 1978;49:5174–87.
- [14] Butt MZ, Feltham P. *J Mater Sci* 1993;28:2557–76.
- [15] Schwartz RB, Labusch R. *J Appl Phys* 1978;49:5174–86.
- [16] Arsenault RJ, Li S. *Metall Trans A* 1989;20A:1429–36.
- [17] Lebyodkin M, Brechet Y, Estrin Y, Kubin L. *Acta Mater* 1996;44:4531–41.
- [18] Zapperi S, Zaiser M. *Mater Sci Eng A* 2001;309–310:348–51.
- [19] Rodary E, Rodney D, Proville L, Bréchet Y, Martin G. *Phys Rev B* 2004;70:054111-1–054111-11.
- [20] Tapasa K, Bacon DJ, Osetsky YN. *Mater Sci Eng A* 2005;400–401:109–13.
- [21] Tapasa K, Bacon DJ, Osetsky YN. *Modell Simul Mater Sci Eng* 2006;14:1153–66.
- [22] Patinet S, Proville L. *Phys Rev B* 2008;78:104109-1–9.
- [23] Proville L, Patinet S. *Phys Rev B* 2010;82:054115-1–054115-19.
- [24] Trinkle DR, Woodward C. *Science* 2005;310:1665–7.
- [25] Yasi JA, Hector Jr LG, Trinkle DR. *Acta Mater* 2010;58:5704–13.
- [26] Zander J, Sandstrom R, Vitos L. *Comput Mater Sci* 2007;41:86–95.
- [27] Zander J, Sandstrom R. *Mater Des* 2008;29:1540–8.
- [28] Leyson GPM, Curtin WA, Hector Jr LG, Woodward CF. *Nat Mater* 2010;9:750–5.
- [29] Basinski ZS, Foxall RA, Pascual R. *Scripta Metall* 1972;6:807–14.
- [30] Kresse G, Hafner J. *Phys Rev B* 1993;47:558–61.
- [31] Kresse G, Furthmuller J. *Phys Rev B* 1996;54:11169–86.
- [32] Vanderbilt D. *Phys Rev B* 1990;41:7892–5.
- [33] Perdew JP, Wang Y. *Phys Rev B* 1992;45:13244–9.
- [34] Perdew JP, Wang Y. *Phys Rev B* 1992;46:12947–54.
- [35] Woodward C, Trinkle DR, Hector Jr LG, Olmsted DL. *Phys Rev Lett* 2008;100:045507-1–4.
- [36] Monkhorst H, Pack J. *Phys Rev B* 1976;13:5188–92.
- [37] Methfessel M, Paxton AT. *Phys Rev B* 1989;40:3616–21.
- [38] Woodward C, Rao SI. *Phys Rev Lett* 2002;88:216402-1–4.
- [39] Hirth JP, Lothe J. *Theory of Dislocations*. 2nd ed. Malabar, FL: Krieger Publishing Company; 1982.
- [40] Vannarat S, Sluiter MHF, Kawazoe Y. *Phys Rev B* 2001;64:224203-1–8.
- [41] Argon AS. *Strengthening Mechanisms in Crystal Plasticity*. New York: Oxford University Press; 2007.
- [42] Labusch R, Grange G, Ahearn J, Haasen P. In: Li JCM, Mukherjee AK, editors. *Rate processes in plastic deformation of materials*. Cleveland, OH: American Society for Metals; 1975.
- [43] Diak BJ, Saimoto S. *Mater Sci Eng A – Struct Mater Prop* 1997;234:1019–22.
- [44] Y. Dong, J. Song, W.A. Curtin, unpublished (2011).
- [45] Diak BJ, Upadhyaya KR, Saimoto S. *Prog Mater Sci* 1998;43:223–363.
- [46] Diak BJ. *Private Commun* 2011.
- [47] Nabarro FRN. *J Less Common Met* 1972;28:257–76.
- [48] Kocks UF, Argon AS, Ashby MF. *Thermodynamics and kinetics of slip*. New York: Pergamon Press; 1975.
- [49] Hardikar K, Shenoy V, Phillips R. *J Mech Phys Solids* 2001;49:1951–67.